Digital simulation of homogeneous chemical reactions coupled to heterogeneous electron transfer and applications at platinum/mica/platinum ultramicroband electrodes

Theresa Varco. Shea, and Allen J. Bard

Anal. Chem., **1987**, 59 (17), 2101-2111 • DOI: 10.1021/ac00144a021

are small enough to permit establishment of a diffusional steady state. In a 1:1, univalent binary electrolyte solution, ohmic potential drops as large as 25 mV may occur near the top of the S-shaped region of a steady-state I-E curve. They should be taken into account prior to any thermodynamic or kinetic analysis. This ohmic potential drop is independent of the concentration of electroactive species. In the presence of supporting electrolyte, the ohmic potential drop is proportional to the ratio of concentrations of the electroactive species to supporting electrolyte but remains independent of electrode geometry. A 50-fold excess of supporting electrolyte reduces the ohmic potential drop to a negligible amount under steady-state potentiostatic conditions. Substantially more supporting electrolyte is required in a rapid scanning triangular wave experiment using a two-electrode technique. The analysis, which is based upon classical limiting law electrochemical transport theory in water, yields a result which does not depend upon the solvent. The latter conclusion is only a first approximation.

ACKNOWLEDGMENT

S.B. thanks J. G. Osteryoung for her valuable and stimulating discussions.

LITERATURE CITED

(1) Wightman, R. M. *Anal. Chem.* **1981**, *53*, 1125A.
(2) Marchiano, S. L.; Arvia, A. J. *Comprehensive Treatise of Electrochemistry*; Yeager, E., Bockris, J. O'M., Conway, B. E., Sarangapani, S., Eds.; Plenum: New York, 1983; Vol. 6, Chapter 2, pp 74-77.
(3) Smythe, W. R. *American Institute of Physics Handbook*, 3rd ed.; Gray, D. E., Ed.; McGraw-Hill: New York, 1972; p 5-12.
(4) Smythe, W. R. *American Institute of Physics Handbook*, 3rd ed.; Gray, D. E., Ed.; McGraw-Hill: New York, 1972; p 5-24.
(5) Ibl, N. *Comprehensive Treatise of Electrochemistry*; Yeager, E., Bockris, J. O'M., Conway, B. E., Sarangapani, S., Eds.; Plenum: New York, 1983; Vol. 6, Chapter 1, pp 42-43.
(6) Bockris, J. O'M.; Reddy, A. K. N. *Modern Electrochemistry*; Plenum: New York, 1972; p 383.

RECEIVED for review February 26, 1987. Accepted April 27, 1987. This work was supported by the Air Force Office of Scientific Research under Grant No. 870037.

Digital Simulation of Homogeneous Chemical Reactions Coupled to Heterogeneous Electron Transfer and Applications at Platinum/Mica/Platinum Ultramicroband Electrodes

Theresa Varco Shea and Allen J. Bard*

Department of Chemistry, University of Texas, Austin, Texas 78712

Digital simulation of generation-collection, shielding, and feedback experiments was carried out for paired ultramicroband electrodes with homogeneous chemical reactions following the heterogeneous electron transfer step, i.e., the EC′ and EC mechanisms. Closely spaced microband electrode pairs were constructed by sputter deposition of Pt onto both sides of 2 to 12 μm thick mica sheets that were mounted between glass slides. The band electrodes thus formed had effective thicknesses of 0.01–6 μm and were 0.5 to 1.2 cm long. Results of cyclic voltammetric and chronoamperometric step, generation-collection, feedback, and shielding experiments with several redox couples agreed with theoretical predictions based on digital simulation of the system at quasi steady state. The application of these band electrodes to the determination of the second-order rate constant for a following catalytic reaction between $Fe(CN)_6^{3-}$ and ascorbic acid or aminopyrine was demonstrated.

We describe here the fabrication of a pair of closely spaced (ca. 2–12 μm) Pt ultramicroband electrodes 0.01–6.0 μm wide by sputter depositing Pt films on mica (*1–3*) and the electrochemical characterization of such electrodes. The application of these electrodes to studies of chemical reactions coupled to a heterogeneous electron transfer reaction, i.e., a following catalytic reaction, by generation–collection experiments under pseudo-first- and second-order reaction conditions is demonstrated. The effects of coupled homogeneous reactions, i.e., the EC′ and EC mechanisms, were studied by digital simulation (*4*) and are reported for two electrode arrays. In particular, generation–collection, shielding, and feedback experiments were simulated.

Ultramicroelectrodes are of interest for several reasons. Steady-state or quasi-steady-state currents are rapidly attained because the small dimensions (less than 10 μm) promote nonlinear mass transport (*5–7*). Moreover, small areas result in low currents allowing the use of microelectrodes in highly resistive media without appreciable iR drops through the solution (*8–11*). Ultramicroelectrodes can also be employed with very fast scan rates in linear sweep voltammetry (*12, 13*) to study nucleation phenomena in electrodeposition (*14–16*) and as electrochemical detectors (*17, 18*). Ultramicroelectrodes of various geometries have been fabricated, including disk electrodes prepared by sealing a fine metal wire or carbon fiber in a glass capillary (*12, 19, 20*), microsphere (*21*), microring (*22, 23*), microband (*24–28*), microcylinder (*29–34*), and vibrating wire electrodes (*35*). Microband electrodes, which consist of a metal film sandwiched between insulators, have been constructed with a metal bandwidth in the nanometer to micrometer range and lengths of 50 μm to several centimeters (*3, 24–28*). Wightman and co-workers describe the construction of a single microband by coating a glass slide with Pt or Au films, sealing this with epoxy cement to a second slide, and using the exposed edge as the electrode (*24, 27*).

While single ultramicroelectrode systems are useful for many types of electrochemical experiments, arrays of two or more closely spaced and independently contacted microelectrodes have also been of interest and can be employed in additional electroanalytical modes. For example, photolithographic techniques can be employed to produce arrays of microband electrodes (*4, 26, 28, 29*), which can be used for electrochemical detectors and in electrogenerated chemiluminescence and electrochemical generation–collection experiments of the type carried out at rotating ring–disk electrodes (RRDE) (*36a, 37*), e.g., with generation of a species at one electrode and subsequent detection of the generated

0003-2700/87/0359-2101$01.50/0

species at the second electrode (*4*).

The paired microband electrode system described here was constructed with an approach similar to that of Wightman et al. (*24*, *27*) and Bond and co-workers (*38*) for single microband electrodes. High-quality mica can be cleaved into very thin sheets that are atomically smooth, and Pt sputtered onto such mica sheets forms a strong adherent film (*1*, *2*). Sputtering onto both sides of a mica sheet yields two Pt films that can be individually contacted to form parallel band electrodes. The microband electrodes described here are 0.5 to 1.2 cm long and nominally 0.01 to 6.0 μm wide (effective areas of 5×10^{-7} to 7×10^{-4} cm^2) separated by mica sheets 2 to 12 μm thick. Cyclic voltammetry and chronoamperometry with several redox couples were used to characterize the behavior of each single microband while generation–collection, shielding (*39*) and feedback experiments were used to characterize the interelectrode gap (*4*, *36a*, *37*). Shielding refers to experiments where the amount of electroactive species reaching one electrode surface is diminished by the amount of reactive species being consumed at the neighboring electrode (*4*, *36a*, *39*). A unique property of microband electrodes when used in a RRDE type generation–collection experiment is the back diffusion of the collected product to the generator, which results in an enhancement of the generator current, the feedback effect.

One advantage of electrode pairs formed by this technique as compared to microelectrodes formed on a substrate is the ready availability of fresh electrode surfaces. The electrode surface can be renewed by simply cutting off the end, in contrast to electrodes formed by lithography, which cannot be polished or subjected to severe forms of surface cleaning and activation (*4*, *26*, *28*). Moreover, fabrication of the electrode pairs does not require cleanroom facilities. The disadvantage of these electrode pairs is the instability of very thin mica sheets to polishing.

Digital simulation techniques have proved very successful in the treatment of electrochemical phenomena, in particular, for systems with kinetic complications (*40–43*) and, more recently, for ultramicroelectrode phenomena (*38*, *44–48*). Where analytical or numerical solutions exist, the results agree quite well with the digital simulations. Digital simulation techniques, however, can be useful for the treatment of electrochemical systems where analytical or numerical solutions do not exist or are not possible (*40–43*). A previously reported digital simulation model has been applied successfully to microband electrodes and can be used to predict the collection efficiency at a pair of electrodes used in the generation–collection mode as well as the shielding and feedback effects (*4*). One of the features of the simulation model is that, unlike other reports of simulations of microband electrodes, cylindrical geometry (*24*, *38*) is not imposed on a rectangular electrode configuration. We report here the modification of the model to include a following catalytic reaction, the EC′ mechanism, which results in enhanced generator currents and diminished collector currents, as well as the EC mechanism which results in diminished generator and collector currents. The simulation model was tested by determining the second-order rate constant for the catalytic reaction between electrogenerated $Fe(CN)_6^{3-}$ and ascorbic acid or aminopyrine at a Pt/mica/Pt electrode pair of known geometry under pseudo-first and second-order reaction conditions.

EXPERIMENTAL SECTION

The construction of the Pt/mica/Pt sandwich structure is shown schematically in Figure 1. The platinum bands were formed by deposition of Pt onto both sides of a freshly cleaved mica sheet (grade 2, ruby c.c.s. mica sheet, United Mineral and Chemical, New York, NY) by rf sputtering at ca. 2×10^{-2} Torr under argon with a Materials Research Corp. (Orangeburg, NY) Model MRC 8620 triple shutter RAD sputtering unit. Platinum

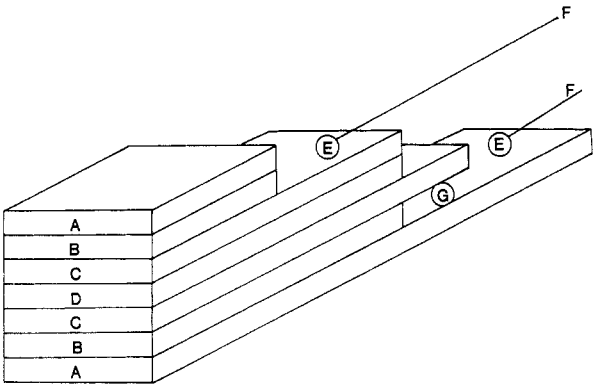

Figure 1. Schematic representation of the Pt/mica/Pt microelectrode pair: A, glass microscope slides; B, epoxy cement; C, Pt film sputtered onto mica; D, mica spacer; E, silver contacts to the Pt on the microscope slide A and the upper Pt film C; F, copper leads; G, graphite contact between first Pt film on mica and Pt film on slide A.

was also sputtered in strips onto glass microscope slides to form one of the electrical contacts to the electrode pair. The sputtering rate (10 Å/s) was measured under the deposition conditions by sputtering Pt for a known time onto glass slides and measuring the absorbance of the resulting metal film, then back calculating the metal thickness.

Electrodes were mounted as shown in Figure 1. After Pt was deposited on both sides of the mica sheet, the mica was cut on all edges with a razor blade, eliminating shorts that occur over the edges of the Pt/mica/Pt sandwich during the sputtering process. Electrical contact between the Pt on the microscope slide and the first Pt layer was made with colloidal graphite (Ted Pella, Inc., Tucson, CA). See Figure 1G. After the Pt was sputtered onto both sides of the mica sheet, the resulting sandwich structure was very fragile; therefore, direct electrical contact to the individual films (e.g., with a wire and silver paint) was not possible without shorting the films together. By making one contact to the Pt on the glass slide with colloidal graphite, additional support was provided for the Pt/mica/Pt pairs. When conductive silver paint was used to make this first contact, shorts developed between the Pt layers during the heating procedure required to set the epoxy. After the graphite was dried in air for 1 to 2 h, the Pt/mica/Pt structure was sealed between two glass microscope slides with optically transparent epoxy (Transcene, Rowley, MA). The epoxy was set (1 h at 80 °C, then 2 h at 140 °C) and copper leads were attached with conductive silver paint (Acme Chemicals and Insulation, Co., New Haven, CT) to the Pt on the microscope slide and to the upper layer of Pt in the Pt/mica/Pt structure; see Figure 1, E and F. The electrical contacts and the upper portion of the sandwich were sealed with 5-min epoxy, and when the electrodes were to be used in nonaqueous solvents, the entire assembly was insulated with silicone sealant. The edges of the electrodes were exposed by cutting away the excess glass at the end with a glass saw. Useful electrode pairs showed a resistance between the Pt electrodes of greater then 20 MΩ. Occasionally, the electrode pair resistance was less than 5 MΩ. In these cases, a voltage was applied between the pair in air with a Harrison 6205B dual dc power supply (Hewlett-Packard, San Diego, CA). The voltage was increased slowly in increments of ca. 1 V (to ca. 10 V) until the measured current dropped to zero, which indicated that the short circuit had been eliminated. The current must be monitored very closely during this operation; too high applied voltages could induce additional shorts. After the Pt/mica/Pt sandwich structure was mounted and the bands were exposed, resistance between the electrodes was measured with a digital multimeter. Good electrode pairs had resistances greater than 20 MΩ in air. To check the contacts between the Pt films and the copper leads, the electrode was immersed in a saturated KCl solution and the resistance between each of the bands and a Pt gauze electrode was measured. Useful electrodes showed resistances of 1 MΩ or less, depending upon the distance between the microband and the Pt gauze electrode. The resistance of the Pt films was very small in good electrodes as measured by contacting the Cu lead and the electrode edge with probes. The contact resistance between the Pt on the glass slide and the Pt

on mica via graphite was typically 50–60 Ω, while the second contact, directly to the Pt on the mica sheet, was less than 10 Ω.

Polishing of the electrode surfaces, i.e., with diamond paste, was generally avoided because such treatments shorted the Pt bands when the interelectrode gap widths were ca. 2–6 μm. However, wider mica spacers were more stable, and electrode pairs with gap widths of ca. 10 μm could be polished with no apparent change in the electrochemistry of a single band electrode, but with changes in the effective gap width as discussed in the results section. Thus, when a fresh electrode surface was needed, the end of the electrode structure was removed with a glass saw and used without further treatment. Electrochemical activation of the electrodes, i.e., cycling in H_2SO_4 between the solvent limits, was avoided because of the instability of thin Pt films on mica during H_2 evolution (*1*, *2*).

Electron micrographs were obtained with a JEOL JSM-35C scanning electron microscope (SEM). X-ray florescence and X-ray mapping were monitored with a KEVEX-XRAY analyzer with a 6900 interface control and 6100 data processor. Samples were mounted with conductive Al tape and coated with ca. 100 Å of Au. Optical micrographs were used to confirm the gap and electrode dimensions obtained by SEM. Optical micrographs were obtained with an Olympus BHTO microscope fitted with an Olympus PM-10AD 35-mm camera (Olympus, Tokyo, Japan) on Kodak Ektachrome 400 film with either vertical or transmission illumination.

Electrochemical measurements were carried out in aqueous solutions purged with nitrogen in the usual three-electrode (single band) or four-electrode (generation–collection) configuration. All chemicals were reagent grade and used without further purification. Solutions were prepared with Milli-Q (18 MΩ) water or reagent grade acetonitrile dried over molecular sieves. Cyclic voltammogram current–voltage curves and potential step current–time transients were recorded with the Soltec X-Y_1Y_2 two-pen recorder with a Princeton Applied Research (Princeton, NJ) Model 175 Universal Programmer and a home-built bipotentiostat (*36b*). Fast scan rate cyclic voltammograms were recorded with a Norland 3001 (Fort Atkinson, WI) digital oscilloscope.

Digital simulations were carried out on the UT-CDC 6000 Dual Cyber Computer (Control Data Corp.) and the Cray-XMP 24 supercomputer (Cray Research, Mendosa Heights, MN).

RESULTS AND DISCUSSION

Digital Simulation of the EC′ and EC Mechanisms. The digital simulation model of generation–collection, shielding, and feedback experiments without coupled kinetics has been reported (*4*) and the modifications necessary to account for the coupled chemical step are given in the Appendix.

Generation–Collection Mode. Generation–collection experiments are described by eq 1 and 2. The collection

$$A \pm ne \rightarrow B \text{ (generator)} \quad (1)$$

$$B \pm ne \rightarrow A \text{ (collector)} \quad (2)$$

efficiency when no homogeneous coupled reactions occur is assumed to occur by a diffusion controlled process, i.e., convection and migration are not important to mass transport. We consider the case of coupled reactions, i.e., the regeneration of A (EC′) or the conversion of B to an electroinactive species (EC), eq 3 and 4, respectively. Both following reactions, EC′

$$\text{EC}' \quad B + Z \xrightarrow{k} A + X \quad \text{(solution)} \quad (3)$$

$$\text{EC} \quad B + Z \xrightarrow{k} Y + X \quad \text{(solution)} \quad (4)$$

and EC, result in the reduction of the collection efficiency when compared to the efficiency observed with no following reaction. The collection efficiency, ϕ_{ss}, is defined as the ratio of the magnitudes of the steady-state or quasi-steady-state currents at the collector (i_C) and the generator (i_G) electrodes, eq 5. Since the following reaction consumes B as it diffuses

$$\phi_{ss} = |i_C|/|i_G| \quad (5)$$

to the collector electrode, i_C is reduced by the reaction. The fraction of B consumed, and the decrease in i_C is a function of the diffusion coefficient, D, the gap width, W_G, and the rate constant, k. The maximum value of ϕ_{ss} (the fraction of B generated that is collected) is a function of D and W_G. The time required for B to diffuse across the gap, t_{Gap}, can be approximated by

$$t_{Gap} = W_{Gap}^2/D \quad (6)$$

This time can be compared to the half-life for the following reaction, t_{rxn}:

$$t_{rxn} = 1/k[Z] \quad (7)$$

When $t_{rxn} \gg t_{Gap}$, the effect of the chemical step is not observed. When $t_{rxn} \ll t_{Gap}$, the collection efficiency approaches zero. At intermediate times, the effect of the following reaction on ϕ_{ss} varies with log λ, the dimensionless rate parameter, eq A15.

The quasi-steady-state collection efficiency is plotted vs. the logarithm of the dimensionless rate parameter, λ, in Figure 2 for a generator single collector electrode configuration. Figure 3 is a plot of ϕ_{ss} vs. λ for small λ. Both the EC′ and EC mechanisms have the same effect on the collection efficiency as a function of λ. Thus, from collection efficiency data, it is possible to measure λ and the reaction rate constant for a following reaction when D and W_{Gap} are known, but it is not

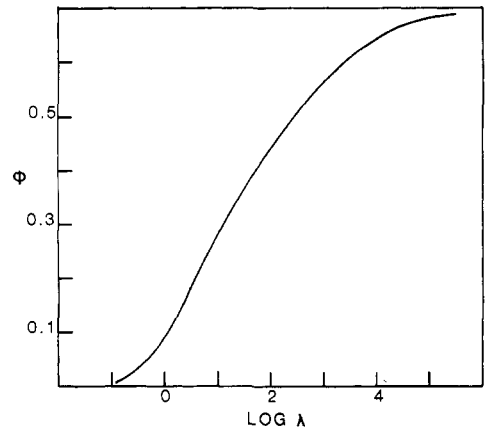

Figure 2. Working curve constructed from digital simulation data for the collection efficiency, ϕ_{ss}, vs. log λ, the dimensionless kinetics parameter $\lambda = (D/W_{Gap,eff})(k_2[Z])^{-1}$.

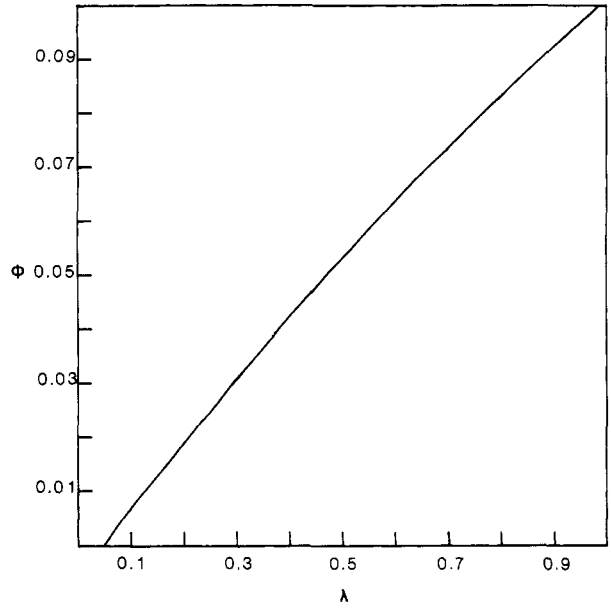

Figure 3. Working curve constructed from digital simulation data for the collection efficiency, ϕ_{ss}, vs. λ, the dimensionless kinetics parameter.

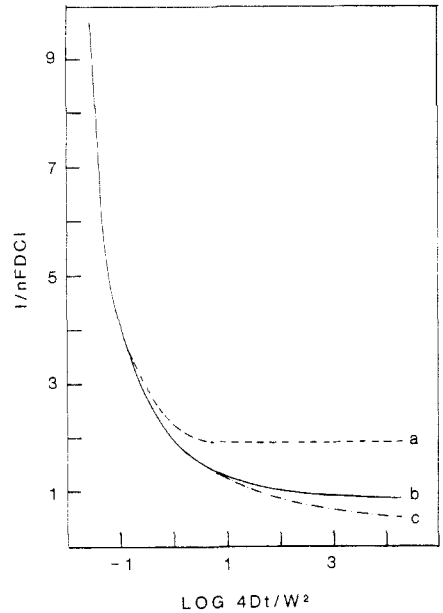

Figure 4. Generator transient (normalized generator current vs. normalized time). *W* is the interelectrode gap width for the generator single collector array: (a) EC′ case; (b) pure diffusion controlled transient; (c) EC case. Curves a and c were calculated with the simulation parameters: L = 750 000; NGAP = NELE = NEB = 6; D_M = 0.24; XKT = 7.5 × 10^{-3}. These parameters are equivalent to k = 2 × 10^3 s^{-1} for a 3.5-s experimental time. λ = 0.89.

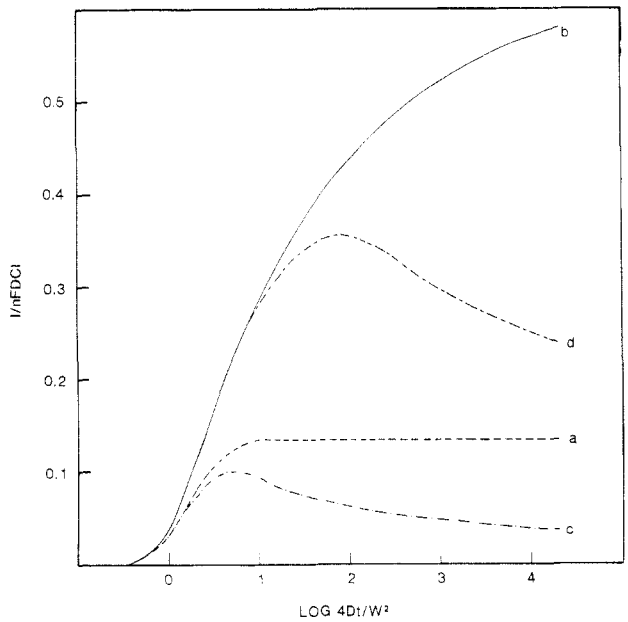

Figure 5. Collector transient (normalized collector current vs. normalized time) where *W* is the interelectrode gap: (a) EC′ case; (b) pure diffusion control; (c) and (d) EC case. Curves a and c correspond to XKT = 7.5 × 10^{-3} (e.g., k = 2 × 10^3 s^{-1} for 3.5 s experimental time). (d) XKT = 2.5 × 10^{-3}. Simulation parameters: L = 750 000; D_M = 0.24; NGAP = NELE = NEB = 6 yielding λ = 0.89 for curves a and c while λ = 2.7 for curve d.

possible to determine the mechanism from ϕ_{ss} alone.

Despite the similarity in the effect of the following reaction on ϕ_{ss}, the EC′ and EC cases can be identified by the current transient at a single microband electrode where an EC′ mechanism results in a steady-state current and the EC transient is the same as the transient in the absence of the following reaction (denoted DP). Moreover, the coupled chemical reaction also alters the generator and collector current transients (Figures 4 and 5). The normalized generator and collector currents are plotted against the logarithm of the dimensionless time parameter, Equation 13. The

Table I. Comparison of Shielding and Feedback Factors for the DP, EC′, and EC Cases as a Function of Time[a]

	SF			FB		
log θ_{Gap}	DP	EC′	EC	DP	EC′	EC
0.6	0.12	0.06	0.12	0.01	0.0	0.01
1.1	0.21	0.06	0.21	0.05	0.01	0.02
2.0	0.30	0.06	0.30	0.17	0.01	0.03
3.0	0.36	0.06	0.36	0.30	0.01	0.04
4.3	0.40	0.06	0.40	0.43	0.01	0.05

[a] Simulation parameters: L = 750 000, D_M = 0.24, NELE = NGAP = NEB = 6, XKT = 7.5 × 10^{-3}.

generator current in the absence of kinetic perturbation is shown as a solid line, Figure 4, curve b. The EC′ reaction results in a true steady-state current which is larger in magnitude than the DP case (curve a). When the EC mechanism obtains, the generator current is smaller, Figure 4, curve c, when compared to the DP current. This difference in the generator currents among the three cases is a manifestation of feedback.

The collector current transients can also be used to distinguish between EC′ and EC controlled kinetics. In Figure 5 the normalized collector current is plotted against the normalized time function, eq 13. In the absence of a homogeneous reaction, the collector current increases until a quasi-steady-state value is attained, Figure 5, curve b. As expected, with the EC′ mechanism, a steady-state current results, curve a, the magnitude depending upon XKT, the normalized rate constant of the reaction (eq A9). As XKT increases, the steady-state collector current decreases.

A distinctive feature of the collector current transient for an EC reaction is the appearance of a peak. The collector currents for the EC case do not attain a quasi-steady-state value, because after the maximum, both the generator and collector currents decay at the same rate. The currents decay rather rapidly, because the amount of feedback is smaller under these conditions than under DP conditions.

Shielding and Feedback Effects under EC′ and EC Control. The shielding effect at the RRDE is a measure of the decrease in the ring current caused by the application of the same potential to the disk (e.g., when $E_D = E_R$) (*39*). The disk reaction shields the ring by decreasing the convective flux of A to the ring electrode. A similar current decrease is observed when adjacent microband electrodes are stepped to the same potential (i.e., $E_G = E_C$). At the microelectrode array, the diffusion layers of adjacent electrodes overlap such that the flux of A to the two electrodes is less than the sum of the fluxes to each of the individual electrodes operated with all other electrodes at open circuit (*4*). The shielding factor, SF, is defined as

$$SF = 1 - i_{sh}/\sum_{j=1}^{n} i_j \qquad (8)$$

where i_{sh} is the shielded current or the total current measured when n electrodes are shorted together and the sum in the denominator is the sum of the currents observed at the n electrodes operated individually in the single electrode mode.

Like the generator and collector currents, the SF varies in a characteristic way with time for the EC′ and EC reaction schemes. Because a true steady state is reached under EC′ conditions for both the single electrode and the generation–collection modes, a similar steady-state behavior for the SF is observed (see Table I). The magnitude of SF depends on the magnitude of k with SF being smaller for the EC′ case than in the absence of kinetic complications.

Shielding at an array of microband electrodes is related to the current response of a single band electrode. Since the

Table II. Limiting Currents: Comparison of Cyclic Voltammetry and Chronoamperometry[a]

	potential step[b]		cyclic voltammetry[c]		theoretical current			
trial no.	i_1, μA	i_2, μA	i_1, μA	i_2, μA	i_1,[d] μA	i_2,[d] μA	i_1,[e] μA	i_2,[e] μA
1	1.24	1.16	1.45	1.14	1.47	1.35	1.80	1.63
2	1.26	1.12	1.39	1.08				
3	1.20	1.10	1.24	1.28				
4	1.21	1.08						
5	1.17	1.08						
6	1.18	1.12						
av	1.21	1.11	1.36	1.17				
std dev	±0.03	±0.03	±0.11	±0.10				

[a] Solution: 5 mM $Ru(NH_3)_6Cl_3$, 0.1 M LiCl. [b] Potential stepped from 0.0 to −0.45 V vs. SCE with the second electrode at open circuit. [c] Potential scanned at 50 mV/s from 0.0 to −0.45 V vs. SCE with the second electrode at open circuit. [d] Theoretical currents calculated by eq 10; with t = 10 s, $D = 7.1 \times 10^{-6}$ cm²/s, l = 1.22 cm, W_1 = 0.12 μm, W_2 = 0.06 μM. [e] Calculated as in d with t = 0.5 s, the characteristic time for the cyclic voltammetry experiment.

current observed at a single microband electrode for the EC case is the same as when no coupled reaction occurs, the SF for the EC mechanism and the DP case is the same. Thus, a distinction between the EC′ and EC mechanisms can be made from the SF.

The feedback factor, FB, is a measure of the amount of A generated from B at the collector, which diffuses back to the generator to react again (no analogous phenomenon exists for the RRDE). The feedback factor is defined as

$$FB = 1 - i_{G,O}/i_{G,C} \quad (9)$$

where $i_{G,O}$ and $i_{G,C}$ are the currents measured at the generator with the collector electrode at open circuit and in the generation–collection modes, respectively. Table I also lists FB for the DP, EC′, and EC cases.

The magnitude of FB is expected to be a function of k for both the EC′ and EC mechanisms. With no following reaction, FB reaches a quasi-steady-state value of ca. 0.43 when $\log \theta_{Gap} = 4.301$. Because the EC′ reaction involves regeneration of A from B (i.e., "chemical feedback"), only a very small feedback effect is observed. For the EC case, FB is smaller than when no reaction occurs. The single electrode current is the same for no kinetic reaction as when the EC mechanism obtains; thus, the numerator in eq 9 is the same for both cases. However, the generator current is larger when no reaction occurs than for the EC case, so that FB is smaller. Thus, digital simulation data presented here can be useful in distinguishing between the EC and EC′ reaction mechanisms as well as measuring the rate constant for a following homogeneous reaction coupled to electron transfer. Steady-state or quasi-steady-state collection efficiencies can be used to calculate k, when D and W_{Gap} are known. The normalized single electrode current transients, the generator and collector current responses, and the shielding and feedback effects can be used to assign the reaction mechanism based on the characteristics of these cases compared to those for the DP case.

Cyclic Voltammetry and Chronoamperometry at Single-Band Electrodes. Each microband electrode was tested separately (i.e., with the second electrode at open circuit) by cyclic voltammetry (CV) and chronoamperometry. Nonlinear diffusion to microband electrodes results in rapid attainment of quasi-steady-state currents so that the limiting current observed should be the same for CV and chronoamperometry. "Quasi-steady-state" is defined for chronoamperometry as the time when there is a change in the normalized current of less than 5% for a 10-fold change in θ (eq 11) (*4*). Similarly the limiting current in cyclic voltammetry should be essentially independent of scan rate (v) for $v \ll (RT/F)(D/W_{eff}^2)$ where D is the diffusion coefficient and W_{eff} is the effective electrode width (*49*). This can be contrasted to the behavior usually found with larger electrodes where the peak current varies as the square root of the scan rate (*36c*).

The experiments summarized in Table II are consistent with these expectations. The limiting current listed for cyclic voltammetry and chronoamperometry (potential step) experiments for a single microband electrode are the same within the error of the experiments for the $Ru(NH_3)_6^{3+}$ couple.

The expression for the quasi-steady-state currents at band electrodes (eq 10) (*50*) was used to calculate the theoretical

$$i = nFDCl(5.553/\ln(\theta) - 6.791/(\ln(\theta))^2) \quad (10)$$

currents in Table II, where n is the number of electrons transferred, F is the Faraday, D is the diffusion coefficient, C is the concentration of electroactive material, and l is the electrode length. The dimensionless parameter, θ, is defined in eq 11, where t is the time in seconds and W is the electrode

$$\theta = 4Dt/W^2 \quad (11)$$

width in centimeters. The currents in the chronoamperometry experiments were measured after t = 10 s, while for cyclic voltammetry, a time (corresponding to RT/Fv) of 0.5 s was used in the calculation. The electrode length was on the order of centimeters, so l was easily determined. The electrode widths estimated by the approximate sputtering rate (10 Å/s) and the sputtering time for this electrode pair were ca. 0.12 and 0.06 μm. When these values are used in the calculations, the theoretical currents were too large when compared to experiment. The theory for microband electrodes and eq 10 strictly apply to rectangular electrodes flush with the substrate surface. The electrodes prepared here, as seen from SEM photographs (Figure 6) are clearly only rough approximations of this geometry. Moreover, portions of the electrode may be covered by bits of epoxy cement. Thus it appears more reasonable to calculate an "effective" electrode width, W_{eff}, based on an electrochemical calibration. With this procedure we find W_{eff} for this electrode pair to be 0.02 and 0.01 μm, respectively. Equation 10 holds for $\theta \geq$ ca. 30 (*50*); for the electrode pair W_{eff} values reported in Table II, this corresponds to times greater than ca. 50 μs.

The SEM micrograph of the Pt/mica/Pt structure given in Figure 6A shows the electrode structure after polishing with 0.25-μm diamond paste. Here the gap and the Pt bands are distinct and well-defined. However, in most cases, the electrodes were used as cut, Figure 6B. The Pt portions, identified by X-ray florescence mapping, are very rough with widely varying widths. In addition, some portions of the electrodes are blocked completely by large pieces of epoxy, which reduce the surface area of the structures from the macroscopically measured one. These irregularities of the Pt/mica/Pt structures can account for the difference between the calculated currents based on estimated widths and the corresponding measured currents. Typically, errors of 20–30% are observed between the measured currents and those calculated

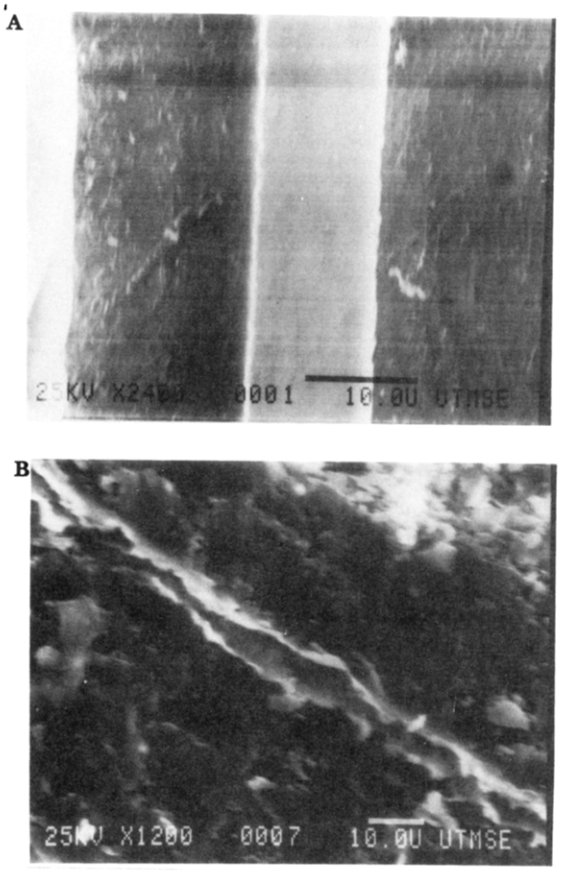

Figure 6. (A) SEM of the Pt/mica/Pt structure with a mica spacer ca. 10 μm wide after polishing with 0.25-μm diamond paste. (B) SEM of the sandwich as cut and used. Pt bands are identified by X-ray florescence mapping. Note the rough edges and nonuniform gap spacing.

from the width estimated by sputtering times.

Treatment of the electrode surface by polishing with 600–200 grit sandpaper as well as with 0.25-μm diamond paste had little effect on the electrochemical response of the Pt/mica/Pt electrode pairs with mica spacers larger than ca. 10 μm when each electrode was used individually, i.e., with the second electrode at open circuit. In some cases the magnitude of the current was reduced after polishing, presumably due to the removal of a few Pt flakes that adhere to the bands (see Figure 6). Figure 7 demonstrates typical effects of polishing the electrodes. Curve A, the current response to a linear voltage sweep at 50 mV/s for a single Pt microband electrode in 5 mM $Ru(NH_3)_6^{3+}$ after cutting with a glass saw, has the sigmoidal shape associated with nonlinear diffusion (*5–7*). Curves B and C were recorded after treatment with 200 and 600 grit sandpaper, respectively. Finally, the electrode was polished on a mechanical polishing wheel with 6-μm diamond paste followed by 1- and 0.25-μm diamond paste (D). Although Figure 7 demonstrates the consistency of the electrochemical behavior with various surface treatments, in general, no polishing treatment was applied after cutting to avoid the possibility of shorting the electrode pairs.

In addition to correcting the electrode width to a W_{eff} to account for geometric irregularities, it would also be possible to correct the electrode length to take account of blocked areas. However, only the effects of nonideal structure on the widths of the electrodes will be considered here, because the bulk of this work is concerned with generation–collection and other two-electrode phenomena where the effects of the interelectrode gap width are probably more important.

The limiting and peak currents at a single microband electrode were studied as a function of the scan rate for scans of 5 mV/s to 20 V/s; the results are summarized in Table III

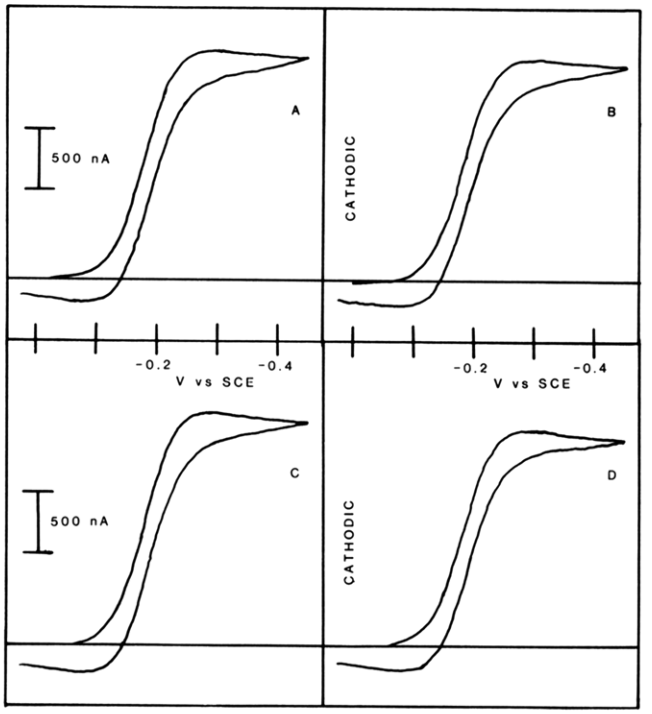

Figure 7. Typical cyclic voltammograms for a microband electrode in 5 mM $Ru(NH_3)_6^{3+}$, 0.1 M LiCl at a sweep rate of 50 mV/s: (A) fresh cut electrode surface; (B) after polishing with 200-grit sandpaper; (C) after 600-grit sandpaper; (D) after polishing with 6-μm, 1-μm, and 0.25-μm diamond paste.

Table III. Effect of Scan Rate on Linear Sweep Voltammetry Maximum (i_l) and Peak (i_p) Currents

scan rate, mV/s	max current,[a] μA	scan rate, V/s	max current,[b] μA
5	5.90	1	2.75
20	6.25	2	4.31
50	6.70	10	13.7
		20	20.3

[a] Potential scanned from 0.0 to 0.7 V vs. SCE in 2.9 mM $K_4Fe(CN)_6$ in 0.3 M glycine, 1 M KOH. [b] Potential scanned from 0.7 to 0.0 V vs. SCE in 5 mM $K_3Fe(CN)_6$ in 1 M aqueous KCl.

for two different electrodes. For scan rates less than ca. 200 mV/s, almost S-shaped curves with limiting current plateaus with no appreciable peak were observed, indicating that the effects of nonlinear mass transport control the current response in this time regime. At the slower sweep rates, the absence of a significant anodic peak on scan reversal (see Figure 7) is characteristic of microelectrodes in which the product diffusion layer thickness is much larger than the electrode dimensions (*7*). Above ca. 1 V/s the voltammograms become peak-shaped with i_p, the peak current, a function of the scan rate (characteristic of mass-transport-controlled conditions in cyclic voltammetry where the diffusion layer thickness is much smaller than the electrode dimensions). The results shown in Table III are consistent with those reported by Bond et al. (*38*) with Au film on glass electrodes 0.05–0.2 μm wide who report "peak" currents which are scan rate dependent at sweeps as slow as 50 mV/s. Wightman (*24, 27*) with similar film electrodes, also reports limiting currents which are scan rate dependent at slow sweep rates ($v < 20$ mV/s). At faster scans, where $v \gg (RT/F)(D/W_{eff}^2)$ diffusion-limited peak currents were observed; these varied with $v^{1/2}$, and the ratio of the anodic to cathodic peak currents was essentially unity as expected for a reversible, diffusion-controlled reaction (*36c*).

Table IV. Comparisons of Electrode Geometries Determined Optically and Electrochemically

electrode	W_G,[a] μm	W_G,[b] μm	$W_{G,eff}$,[c] μm	electrode width, μm: estimated[d] 1	estimated[d] 2	effective[e] 1	effective[e] 2	length,[f] cm
1[g]	10	12	50	0.12	0.06	0.02	0.01	1.22
2[g]		7	20	0.06	0.12	0.01	0.01	0.68
3	6	5	4	0.36	0.60	1.5	4.2	0.50
4	2	4	2.5	0.36	0.60	0.18	5.7	1.15
5		6	7.5	0.36	0.60	0.90	1.8	0.71

[a] Average determined by SEM. [b] Average determined by optical microscopy. [c] Calculated from eq 12 and 13 with φ measured in 5 mM $Ru(NH_3)_6Cl_3$ in 0.1 M aqueous LiCl and 2 mM $K_4Fe(CN)_6$ in 0.7 M aqueous KOH 10 s after potential step. [d] Estimated from the sputtering time and the approximate sputtering rate (10 Å/s). [e] Calculated by eq 10 and 11 at 10 s after a potential step in 5 mM $Ru(NH_3)_6Cl_3$ in 0.1 M aqueous LiCl. [f] Measured by ruler. [g] Sanded with 200- and 600-grit sandpaper before use.

Thus, ultramicroband electrodes formed by sputter deposition of Pt onto mica sheets show the expected behavior when used as single working electrodes in the usual three-electrode configuration. Although each band has a very irregular geometry, the electrochemical responses can be used to estimate an effective width based on eq 10 and 11 for the current at an ideal microband electrode. Further characterization of the electrode pairs was carried out in the dual band generation–collection mode.

Dual Band Modes. The electrode pairs were tested in generation–collection, shielding, and feedback experiments with reversible couples in aqueous solution at sufficiently long times or slow scan rates that quasi-steady-state currents were observed. The experimental results of generation–collection experiments were used to estimate effective gap widths, $W_{Gap,eff}$, in a calculation similar to that used to estimate an effective electrode width.

Theoretical gap widths, $W_{Gap,eff}$, were calculated by solving eq 12 for θ_{Gap}, eq 13. Equation 12 is an empirical expression

$$\phi_{ss} = 0.033 + 0.21 \log \theta_{Gap} - 0.016(\log \theta_{Gap})^2 \quad (12)$$

$$\theta_{Gap} = 4\,Dt/W^2_{Gap} \quad (13)$$

derived from digital simulation results relating the measured collection efficiency to the electrode geometry, the experimental time, and diffusion coefficient and has been shown to predict the collection efficiency for well-defined electrode geometries (*4*). The quasi-steady-state collection efficiency, ϕ_{ss}, was measured with several reversible redox couples. Effective gap widths determined from ϕ_{ss} as well as the gap width measured by SEM and optical microscopy are listed in Table IV. Good agreement between the experimental determinations of the interelectrode spacing was found for electrodes that were cut and not polished (electrodes 3–5); deviation between the SEM and optical measurements was generally 1–2 μm. Electrodes 1 and 2, however, show very large effective gap widths compared to the microscopically measured interelectrode spacing. Electrodes 1 and 2 had been sanded with 200- and 600-grit sandpaper to renew the surfaces before use while electrodes 3–5 were simply cut without further polishing. The uneven removal of Pt, mica, glass, and epoxy may increase the effective gap width as shown schematically in Figure 8. Previously (*4*), eq 12 had been shown to be accurate (to within 10%) for log θ between 1.8 and 5.7 and the electrode dimensions and times reported in Table IV are within these limits.

Also summarized in Table IV are the electrode widths estimated by sputtering time and the effective electrode widths as determined from the limiting currents. The large difference between the two measurements can be attributed to errors in estimating the electrode width by sputtering rates, which may vary at long times, and the previously discussed geometric factors.

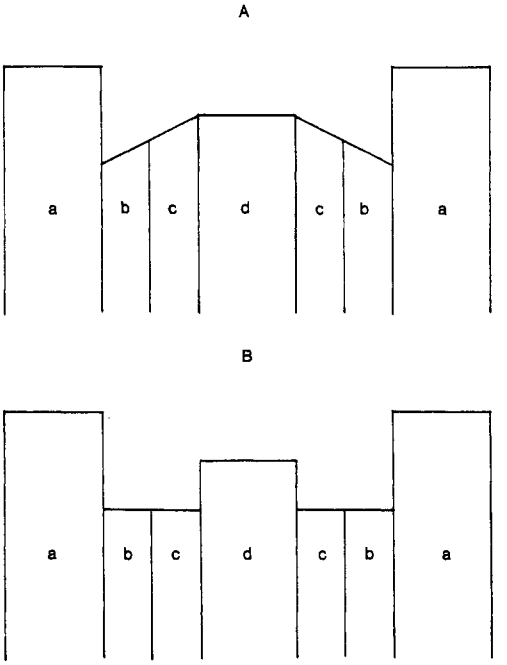

Figure 8. Schematic of the possible effects of polishing showing the uneven removal of glass (a), epoxy (b), Pt (c), and mica (d), resulting in an increased effective gap width ($W_{Gap,eff}$) between the Pt bands (c).

Electrochemical characterization of pairs of ultramicroband electrodes, including collection, feedback, and shielding experiments, for four electrodes that were freshly cut but otherwise untreated before use in different solutions are shown in Table V. Currents were measured 10 s after a potential step to the generator electrode, while the collector electrode potential was maintained at the initial generator electrode potential (collection and feedback) or stepped to the same potential (shielding). The collection efficiency was measured and log $\theta_{Gap,eff}$ was determined from eq 12. This was used to estimate the feedback factor, FB, and the shielding factor, SF, from simulation data (*4*).

Feedback factors for pairs of electrodes and theoretical values in two different solutions are compared in Table V. The agreement between the experimental data and simulation predictions is inconsistent. In most cases the experimental feedback effect was smaller than the theory predicted, even though the effective interelectrode gap width, estimated by the collection efficiency, was used in the calculation. Shielding factors are also listed in Table V. For these, experimental and simulated values are probably within the errors of the experiments and simulation.

Following Catalytic Reaction—Rate Constant by Collection Measurements. Ultramicroelectrode arrays can also be employed to study homogeneous reactions coupled to the electron transfer by measuring the collection efficiency

Table V. Summary of Collection Efficiency, Shielding, and Feedback for Reversible Redox Couples

electrode	collection efficiency ϕ_{SS}	log θ_{Gap}	shielding factor		feedback factor	
			exptl	simulation	exptl	simulation
			(a) $Ru(NH_3)_6^{3+}$ Solution			
3	0.565 ± 0.002	3.43	0.355 ± 0.015	0.357	0.266 ± 0.003	0.311
4	0.611 ± 0.005	3.93	0.280 ± 0.008	0.364	0.212 ± 0.003	0.371
5	0.528 ± 0.005	3.08	0.314 ± 0.007	0.347	0.278 ± 0.003	0.270
6	0.356 ± 0.001	1.78	0.253 ± 0.005	0.265	0.080 ± 0.004	0.127
			(b) $Fe(CN)_6^{4-}$ Solution			
3	0.518 ± 0.033	2.99	0.359 ± 0.018	0.344	0.271 ± 0.003	0.260
4	0.556 ± 0.013	3.34	0.263 ± 0.019	0.355	0.085 ± 0.021	0.300
5	0.447 ± 0.012	2.42	0.327 ± 0.033	0.314	0.140 ± 0.011	0.196
6	0.390 ± 0.004	1.95	0.211 ± 0.008	0.287	0.054 ± 0.005	0.145

in an approach analogous to RRDE studies (*37*). The digital simulation model (*4*) was modified to treat a following catalytic second-order and pseudo-first-order (EC′) reaction; details are given in the Appendix. We consider here the EC′ case under the conditions where Z is present at concentrations of the order of those of A and a complete second-order reaction treatment must be carried out, and when [Z] ≫ [A], so that k_2[Z] remains essentially constant and the reaction can be treated as a pseudo-first-order reaction. We illustrate this case experimentally with species A corresponding to $Fe(CN)_6^{4-}$, B, the oxidized form, $Fe(CN)_6^{3-}$, and Z either ascorbic acid (*51*, *52*) or aminopyrine (1-phenyl-2,3-dimethyl-4-(dimethylamino)-5-pyrazolone) (*53*, *54*). Both ascorbic acid and aminopyrine are oxidized by ferricyanide in solution with rate constants for the second-order reaction differing by nearly 2 orders of magnitude. The potential of the generator electrode was controlled to minimize direct oxidation of ascorbic acid or aminopyrine at the surface.

The effect of the following reaction is to increase the oxidation currents at a single band electrode or a generator electrode when the electrode pair is used in the generation–collection mode and to decrease the collector current. In this way the observed collection efficiency will be decreased by the amount of $Fe(CN)_6^{3-}$ consumed during the time it diffuses across the interelectrode gap. The amount of $Fe(CN)_6^{4-}$ regenerated in the whole diffusion layer surrounding the generator electrode increases the generator current. From the digital simulations of the electrode pairs under pseudo-first-order conditions, working curves of the collection efficiency, ϕ_{ss}, as a function of λ, a dimensionless rate parameter, eq A15, were constructed, Figures 2 and 3.

Experimentally, ϕ_{ss} was determined without Z present, and from eq 12, the effective gap width, $W_{Gap,eff}$, was determined. Then, ϕ_{ss} was determined at known concentrations of Z. From ϕ_{ss}, a value of λ was found and eq A15 was solved for k_2. The data shown in Tables VI and VII are from two sets of experiments for the determination of k_2 for the reaction of $Fe(CN)_6^{3-}$ with ascorbic acid and aminopyrine, respectively.

For the reaction with ascorbic acid, the solution was buffered with glycine (0.3 M) and the pH was adjusted to 2.5 with nitric acid (*51*, *52*). The ratio of Z concentration to the bulk concentration of the reduced species was varied from ca. 5.70 to 78.0 (Table VI). In an experiment with only $Fe(CN)_6^{4-}$ present, the collection efficiencies were measured at t = 3.5 s. Equations 12 and 13 were used to obtain the value of $D/W_{Gap,eff}$. The reactant (Z) was then added and ϕ_{ss} was determined again. The values of k_2 determined are in reasonable agreement but slightly higher than the values measured by spectroelectrochemical methods, 13.6 ± 0.2 L mol^{-1} s^{-1} at pH 2.2 (*51*) and 23.6 ± 2.4 L mol^{-1} s^{-1} at pH 2.5 (*52*). Part of the error in this work was caused by the background correction for a solution of ascorbic acid alone, which must be obtained with a fresh solution. In addition, the electrodes were not very stable in the acidic solutions over long periods of time.

Table VI. Generation–Collection Data for the Determination of the Second-Order Rate Constant of Ferricyanide Reduction by Ascorbic Acid[a]

[ascorbic acid], mM	ϕ	λ	k_2, L mol^{-1} s^{-1}	C_Z/C_A
0	0.247			0
8.77	0.120	1.86	30	5.70
12.8	0.100	1.24	29	8.83
25.7	0.071	0.91	20	17.7
0	0.346			0
51.5	0.013	1.28	28	78.0
av			27	
std dev			±4	

[a] Solution is 1 to 3 mM $K_4Fe(CN)_6$ in 0.3 M glycine at pH 2.5. Freshly cut electrode no. 6.

Table VII. Generation–Collection Data for the Determination of the Second-Order Rate Constant for the Reduction of Ferricyanide by Aminopyrine[a]

[aminopyrine], mM	ϕ	λ	k_2, L mol^{-1} s^{-1}	C_Z/C_A
0	0.389			0
10.3	0.173	2.76	9×10^2	5.5
21.7	0.127	1.65	7×10^2	11.3
0	0.382			0
13.1	0.140	1.90	9×10^2	11.3
0	0.298			0
40.4	0.019	0.202	8×10^2	31.3
av			8×10^2	
std dev			±1	

[a] Solutions are 1 to 5 mM $K_4Fe(CN)_6$ in 1 M aqueous KOH. Freshly cut electrode no. 6.

Table VII lists the data obtained for the reduction of $Fe(CN)_6^{3-}$ by aminopyrine in basic solution (*53*, *54*). The ratio of the concentration of Z to reduced species was varied from ca. 5.5 to 31.3. The maximum concentration of aminopyrine used was ca. 40 mM because of its limited solubility in water. The rate constant for this reaction, (8 ± 1) × 10^2 L mol^{-1} s^{-1} is in fairly good agreement with previously reported values (1 to 3 × 10^3 L mol^{-1} s^{-1}) (*53*, *54*). The somewhat smaller values may be due to the incomplete dissolution of the catalyst, resulting in the actual concentrations being lower than those listed in Table VII. Because of the small background currents measured in solutions with Z alone at these potentials, no correction was made for the oxidation of aminopyrine at the generator.

The determination of second-order homogeneous rate constants under pseudo-first-order conditions is shown here

Table VIII. Simulation of the Catalytic Regeneration of Ferrocyanide under Second-Order Reaction Conditions

Ascorbic Acid[a]

concn[b]	ϕ_{ss} exptl	ϕ_{ss} simulation
0	0.367	
2.3	0.166	0.178
3.0	0.148	0.146
3.7	0.133	0.124

concn[d]	ϕ_{ss} exptl	ϕ_{ss} simulation
Aminopyrine[c]		
0	0.355	
0.7	0.138	0.168
1.6	0.119	0.119
2.3	0.108	0.091

[a] Solution: 2.90 mM $K_4Fe(CN)_6$ in 0.3 M glycine at pH 2.5, $W_{Gap,eff}$ = 18 μm. Simulation: D_M = 0.24, NGAP = 20, XKTC = 10^{-4}. [b] Concn = 2[ascorbic acid]/[$K_4Fe(CN)_6$]. [c] Solution: 2.64 mM $K_4Fe(CN)_6$ in 1 M KOH, $W_{Gap,eff}$ = 19 μm. Simulation: D_M = 0.24, NGAP = 35, XKTC = 10^{-4}. [d] Concn = [aminopyrine]/[$K_4Fe(CN)_6$].

to be relatively straightforward and fairly accurate with the electrode pairs constructed based on a mica spacer. If we assume that 0.2 μm is a practical lower limit for the interelectrode gap width (*4*), a diffusion coefficient, D, of ca. 5 × 10^{-6} cm²/s, and a lower limit of measurable ϕ_{ss} of ca. 0.001, then with a λ of 0.056 a $k_2[Z]$ of the order of 10^5 s^{-1} is measurable. Thus for Z concentrations of 10^{-3} to 10^{-2} M, the upper limits of measurable rate constants are about 10^7 to 10^8 L mol^{-1} s^{-1}. In practice it may be possible to measure efficiencies less than 0.001, since the collector currents measured to determine the collection efficiencies in Tables VI and VII were of the order of 100 nA and the measured current can be increased by increasing the electrode length. Thus, it may be possible to measure very fast rate constants, up to diffusion limited processes, with ultramicroelectrode arrays.

Comparison of the Simulation and Experimental Collection Efficiencies under Second-Order Conditions. The simulation modifications necessary to include the following catalytic reaction under second-order conditions are also included in the Appendix. From the data obtained under pseudo-first-order conditions, the rate constants for the reaction of ferricyanide with ascorbic acid or aminopyrine were determined.

Experimentally, the concentration of Z was varied for a constant bulk concentration of ferrocyanide. The collection efficiency was measured both with and without Z. From ϕ_{ss} and eq 12 and 13 the effective gap width was determined without Z. The collection efficiencies and the concentrations are listed in Table VIII. The experimentally measured D,$W_{Gap,eff}$, k_2, and C_A can be used to calculate a value for the second-order rate parameter, λ_2. The simulation value of XKTC is fixed once the values of D_M and NGAP are selected. The maximum value of D_M is 0.25, further restricting the range of values of NGAP and XKTC possible.

Once the simulation parameters, D_M, NGAP, and XKTC were determined, the final input parameter, CONC, the ratio of Z to A, was determined and the simulation run. Comparisons of the experimental and simulation ϕ_{ss} values under second-order conditions are presented in Table VIII. Generally very good agreement between simulation and experimental results is found.

Electrode Stability in Aqueous Solutions. The stability of the electrode pairs after immersion in various solutions was determined by the reproducibility of the collection efficiency and the current function, i/CD, with time (where i is the maximum or limiting current and C the concentration of redox material). The current function changed by only 2% to 3% for electrodes used in different neutral or basic solutions over the course of 10 days without resurfacing (i.e., without cutting a fresh surface). When a fresh surface was cut, however, electrodes experienced up to a 22% change in the current function, presumably because of changes in W_{eff}. However, the observed collection efficiencies during this time frame were the same within 11–13% for nonresurfaced and for fresh cut electrodes. Thus, resurfacing may cause significant changes in the effective areas of the electrodes, but the relatively small changes in ϕ_{ss} suggest that the effective interelectrode gap width remains fairly constant. However, irreproducible behavior was observed at pH 2.5 after only 1–2 h of use. This is caused by the instability of Pt on mica which is known to flake during H_2 evolution (*1*, *2*) and also on long immersion in acidic solutions (pH <3). Removal of the electrode end with a glass saw generates a new electrode surface and results in a new stable electrode. In general, electrode pairs as constructed here have been used for several months without any major changes in the electrochemical performance.

Use in Nonaqueous Solvents. Preliminary studies of the reduction of $Ru(bpy)_3^{2+}$ in acetonitrile (MeCN) solution demonstrated that it is possible to conduct generation–collection experiments of the type previously described with $Ru(bpy)_3^{2+}$. The reduction of the solvent must be carefully avoided to prevent the formation of a yellowish brown film that shorts the two bands. The epoxy used to mount the electrodes was stable for at least several hours in MeCN.

CONCLUSIONS

We have demonstrated here that pairs of ultramicroelectrode bands can be constructed by sputter deposition of Pt films onto a mica spacer 2 to 12 μm thick and that each band is individually addressable. The electrode pairs can be used in generation–collection experiments similar to an RRDE and to measure the homogeneous second-order rate constant for a catalytic following reaction under pseudo-first- and second-order reaction conditions. The digital simulation model presented previously (*4*) and modified here successfully predicts collection and shielding effects, and working curves constructed from the model can be used to determine rate constants. Moreover, simulation results show that SF, FB, and the current transient shapes can be used to distinguish the EC′ and EC reaction mechanisms using electrode pairs as described here. The advantages of the electrodes constructed as described here include long lifetimes and renewable electrode surfaces, but their geometries are less well-defined than those prepared by photolithography.

Pairs of ultramicroelectrodes were demonstrated to be useful for the determination of the second-order rate constant for a following catalytic reaction in experiments similar to those carried out at an RRDE (*36a*, *37*, *39*). An additional advantage to using arrays for studying the effects of chemical reactions coupled to heterogeneous charge transfers is that, like the RRDE, the arrays should be useful for distinguishing between the EC and EC′ mechanisms by the effect of the reaction on the generator current.

ACKNOWLEDGMENT

The authors thank J. M. Davis and S. Feldberg for helpful discussions.

APPENDIX

Modification of the Digital Simulation Model To Include the Following Chemical Reactions. The digital simulation model used to describe generation and collection of a reversible couple at a pair of ultramicroband electrodes

has been described in detail (*4*). A two-dimensional exponentially expanding space grid (*55*, *56*) from a single generator, single collector electrode arrangement was used here and only the modifications necessary to describe the following chemical steps will be discussed. A complete listing of the program is available (*57*). The total number of iterations, L, the dimensionless rate constants, XKT and XKTC, and the number of boxes representing the collector electrode and the interelectrode gap NEB and NGAP were varied; the number of boxes representing the generator electrode surface, NELE, was held constant. When the maximum number of iterations was changed from 750 000 to 93 300, the results were the same to <3%, because the system reaches true steady state very rapidly with the catalytic follow up reaction. The reaction schemes considered are shown in eq 1 to 4 in the text. The rate law governing the conversion of B to A by Z is

$$-\mathrm{d[B]}/\mathrm{d}t = -\mathrm{d[Z]}/\mathrm{d}t = \mathrm{d[A]}/\mathrm{d}t = k_2\mathrm{[Z][B]} \quad \text{(A1)}$$

and for the conversion of B to Y by Z

$$-\mathrm{d[B]}/\mathrm{d}t = -\mathrm{d[Z]}/\mathrm{d}t = \mathrm{d[Y]}/\mathrm{d}t = k_2\mathrm{[Z][B]} \quad \text{(A2)}$$

When pseudo-first-order conditions obtain, i.e., [Z] ≫ [A], k_2[Z] ≈ k', (A3) results.

$$-\mathrm{d[B]}/\mathrm{d}t = \mathrm{d[A]}/\mathrm{d}t = k'\mathrm{[B]} \quad \text{(A3)}$$

The finite difference form of (A3) after normalizing the concentrations in terms of the bulk concentration of A and multiplying through by Δt results in eq A4 or A5, where

$$-\Delta C_B(N,J) = \Delta C_A(N,J) = k'\Delta t C_B(N,J) \quad \text{(EC')} \quad \text{(A4)}$$

$$-\Delta C_B(N,J) = k'\Delta t C_B(N,J) \quad \text{(EC)} \quad \text{(A5)}$$

$C_B(N,J)$ is the concentration of B in the box, N,J after the diffusion step and $\Delta C_B(N,J)$ and $\Delta C_A(N,J)$ are the changes in concentration in the box N,J caused by the homogeneous regeneration reaction and (A5) is the concentration change for the EC mechanism. From the definition of the simulation maximum number of iterations, L, and a final experimental time, t_F, the simulation time increment Δt is known

$$\Delta t = t_F/L = t/K \quad \text{(A6)}$$

Substitution of (A6) into (A4) or (A5) yields (A7) or (A8), the change in concentration in terms of the normalized concentrations

$$-\Delta C_B(N,J) = \Delta C_A(N,J) = C_B(N,J)\,(k't_F/L) \quad \text{(EC')} \quad \text{(A7)}$$

$$-\Delta C_B(N,J) = C_B(N,J)(k't_F/L) \quad \text{(EC)} \quad \text{(A8)}$$

We define the dimensionless simulation rate constant, XKT, as

$$\mathrm{XKT} = k't_F/L \quad \text{(A9)}$$

Modifications of the concentrations in each box caused by the following reaction were made after the concentration changes caused by diffusion were calculated. The equations for the diffusional changes have been given previously (4) and eq A10 and A11 describe the concentration changes caused by the homogeneous catalytic reaction. Only eq A11 applies for the EC case.

$$C_{A,NEW}(N,J) = C_{A,NEW}(N,J) + \mathrm{XKT}\ C_{B,NEW}(N,J) \quad \text{(EC')} \quad \text{(A10)}$$

$$C_{B,NEW}(N,J) = C_{B,NEW}(N,J) - \mathrm{XKT}\ C_{B,NEW}(N,J) \quad \text{(EC and EC')} \quad \text{(A11)}$$

Previously, eq A12 was shown to hold as a conversion between the real world variables D, t, and W_{Gap}, where D is the diffusion coefficient in cm²/s, t is time in s, and W_{Gap} is the gap width in cm, and the corresponding simulation variables D_M, K, and NGAP (the dimensionless diffusion constant, the iteration counter, and the number of boxes corresponding to the gap width, respectively).

$$4Dt/W_{Gap}^2 = 4D_MK/\mathrm{NGAP}^2 \quad \text{(A12)}$$

From (A12) and (A6)

$$D_M/\mathrm{NGAP}^2 = Dt/W_{Gap}^2K = D\Delta t/W_{Gap}^2 \quad \text{(A13)}$$

and with (A9)

$$D_M/\mathrm{NGAP}^2 = Dt_F/W_{Gap}^2L = D(\mathrm{XKT})/W_{Gap}^2k' \quad \text{(A14)}$$

We define the dimensionless rate parameter, λ, in (A15)

$$\lambda = D_M/\mathrm{NGAP}^2\mathrm{XKT} = D/W_{Gap}^2k_2' = D/W_{Gap}^2k\mathrm{[Z]} \quad \text{(A15)}$$

When second-order kinetics apply, the treatment is similar to that for pseudo-first-order kinetics; however, the effects of diffusion of Z must be calculated throughout the simulation, with the relative concentration of Z normalized by the bulk concentration of A initially present; the ratio of the concentrations is supplied as an input parameter in the simulation. The initial concentration of Z in the simulation is defined as CONC

$$\mathrm{CONC} = \mathrm{[Z]}/\mathrm{[A]}_{bulk} \quad \text{(A16)}$$

The rate law, eq A1 in finite difference form becomes eq A17 after dividing through by the bulk concentration of A

$$-\Delta C_B(N,J) = -\Delta C_Z(N,J) = \Delta C_A(N,J) = k_2\Delta t\mathrm{[Z]}C_B(N,J) \quad \text{(A17)}$$

Equation A17 is multiplied and divided by the bulk concentration of A, C_A*, to normalize the concentration of Z on the right-hand side resulting in

$$-\Delta C_B(N,J) = -\Delta C_Z(N,J) = \Delta C_A(N,J) = k_2\Delta t C_A^* C_B(N,J)C_Z(N,J) \quad \text{(A18)}$$

The dimensionless rate constant XKTC is defined

$$\mathrm{XKTC} = k_2\Delta t C_A^* = k_2 t_F C_A^*/L \quad \text{(A19)}$$

By substitution of Δt from (A6) into (A19), one obtains

$$\lambda_2 = D_M/\mathrm{NGAP}^2\ \mathrm{XKTC} = D/W_{Gap}^2\ \ k_2C_A^* \quad \text{(A20)}$$

Registry No. Pt, 7440-06-4; $Fe(CN)_6^{3-}$, 13408-62-3; $Ru(NH_3)_6^{3+}$, 18943-33-4; ascorbic acid, 50-81-7; aminopyrine, 58-15-1.

LITERATURE CITED

(1) Liu, H.-Y.; Fan, F.-R. F.; Bard, A. J. *J. Electrochem. Soc.* **1985**, *132*, 2666.
(2) Maeda, M.; White, H. S.; McClure, D. J. *J. Electroanal. Chem.* **1986**, *200*, 383.
(3) Morris, R. B.; Franta, D. J.; White, H. S., submitted.
(4) Bard, A. J.; Crayston, J. A.; Kittlesen, G. P.; Varco Shea, T.; Wrighton, M. S. *Anal. Chem.* **1986**, *58*, 2321.
(5) Hepel, T.; Osteryoung, J. *J. Phys. Chem.* **1982**, *86*, 1406.
(6) Aoki, K.; Osteryoung, J. *J. Electroanal. Chem.* **1981**, *122*, 19.
(7) Wightman, R. M. *Anal. Chem.* **1981**, *53*, 1125A.
(8) Bond, A. M.; Fleischmann, M.; Robinson, J. *J. Electroanal. Chem.* **1984**, *172*, 11.
(9) Bond, A. M.; Fleischmann, M.; Robinson, J. *J. Electroanal. Chem.* **1984**, *168*, 299.
(10) Thormann, W.; van den Bosch, P.; Bond, A. M. *Anal. Chem.* **1985**, *57*, 2764.
(11) Bond, A. M.; Lay, P. A. *J. Electroanal. Chem.* **1986**, *199*, 285.
(12) Howell, J. O.; Wightman, R. M. *J. Phys. Chem.* **1984**, *88*, 3915.
(13) Montenegro, M. I.; Pletcher, D. *J. Electroanal. Chem.* **1986** *200*, 371.
(14) Scharifker, B.; Hills, G. *J. Electroanal. Chem.* **1981**, *130*, 81.
(15) Gunawardena, G.; Hills, G.; Scharifker, B. *J. Electroanal. Chem.* **1981**, *130*, 99.
(16) Hills, G.; Pour, A. K.; Scharifker, B. *J. Electrochim. Acta* **1983**, *28*, 891.
(17) Ghorochian, J.; Sarfarazi, F.; Dibble, T.; Cassidy, J.; Smith, J. J.; Russell, A.; Dunmore, G.; Fleischmann, M.; Pons, S. *Anal. Chem.* **1986**, *58*, 2276.
(18) Fosdick, L. E.; Anderson, J. L. *Anal. Chem.* **1986**, *58*, 2481.

(19) Dayton, M. A.; Brown, J. C.; Stutts, K. J.; Wightman, R. M. *Anal. Chem.* **1980**, *52*, 946.
(20) Dayton, M. A.; Ewing, A. G.; Wightman, R. M. *Anal. Chem.* **1980**, *52*, 2392.
(21) Wehmeyer, K. R.; Wightman, R. M. *Anal. Chem.* **1985**, *57*, 1989.
(22) Kim, Y.-T.; Scarnulis, M.; Ewing, A. G. *Anal. Chem.* **1986**, *58*, 1782.
(23) McFarlane, D. R.; Wong, D. K. Y. *J. Electroanal. Chem.* **1985**, *185*, 197.
(24) Wehmeyer, K. R.; Deakin, M. R.; Wightman, R. M. *Anal. Chem.* **1985**, *57*, 1913.
(25) Saito, Y. *Rev. Polarogr.* **1968**, *15*, 177.
(26) Kittlesen, G. P.; White, H. S.; Wrighton, M. S. *J. Am. Chem. Soc.* **1984**, *106*, 7389.
(27) Kovach, P. M.; Caudill, W. L.; Peters, D. G.; Wightman, R. M. J. *Electroanal. Chem.* **1985**, *185*, 285.
(28) White, H. S.; Kittlesen, G. P.; Wrighton, M. S. *J. Am. Chem. Soc.* **1984**, *106*, 5375.
(29) Sanderson, D. G.; Anderson, L. B. *Anal. Chem.* **1985**, *57*, 2388.
(30) Sujaritvanichpong, S.; Aoki, K.; Tokuda, K.; Matsuda, H. *J. Electroanal. Chem.* **1986**, *199*, 271.
(31) Aoki, K.; Honda, K.; Tokuda, K.; Matsuda, H. *J. Electroanal. Chem.* **1985**, *182*, 267.
(32) Amatore, C. A.; Deakin, M. R.; Wightman, R. M. *J. Electroanal. Chem.* **1986**, *206*, 23.
(33) Aoki, K.; Tokuda, K.; Matsuda, H. *J. Electroanal. Chem.* **1986**, *206*, 47.
(34) Kovach, P. M.; Deakin, M. R.; Wightman, R. M. *J. Phys. Chem.* **1986**, *90*, 4612.
(35) Schuette, S. A.; McCreery, R. L. *Anal. Chem.* **1986**, *58*, 1778.
(36) Bard, A. J.; Faulkner, L. R. In *Electrochemical Methods, Fundamentals and Applications*; Wiley: New York, 1980; (a) pp 300–304, (b) p 567 with some modification, (c) p 219.
(37) Aubery, W. J.; Hitchman, M. L. In *Ring-Disc Electrodes*; Clarendon Press, Oxford University Press: London, 1971.
(38) Bond, A. M.; Henderson, T. L. E.; Thormann, W. *J. Phys. Chem.* **1986**, *90*, 2911.
(39) Bruckenstein, S.; Miller, B. *Acc. Chem. Res.* **1977**, *10*, 54.
(40) Britz, D. In *Digital Simulation in Electrochemistry*; Springer-Verlag: New York, 1981; p 74.
(41) Feldberg, S. W. In *Electroanalytical Chemistry*; Bard, A. J., Ed.; Marcel Dekker: New York, 1969; Vol. 3.
(42) Prater, K. B. In *Electrochemistry Calculations, Simulation and Instrumentation*; Mattson, J. S., Mark, H. B., MacDonald, H. C., Jr., Eds.; Marcel Dekker: New York, 1972; Vol. 2.
(43) Maloy, J. T. In *Laboratory Techniques in Electroanalytical Chemistry*; Kissinger, P. T., Heineman, W. R., Eds.; Marcel Dekker: New York, 1984.
(44) Flanagan, J. B.; Marcoux, L. *J. Phys. Chem.* **1973**, *77*, 1051.
(45) Heinze, J. *J. Electroanal. Chem.* **1981**, *124*, 73.
(46) Reller, H.; Kirowa-Eisner, E.; Gileadi, E. *J. Electroanal. Chem.* **1984**, *161*, 247.
(47) Reller, H.; Kirowa-Eisner, E.; Gileadi, E. *J. Electroanal. Chem.* **1982**, *138*, 65.
(48) Shoup, D.; Szabo, A. *J. Electroanal. Chem.* **1982**, *140*, 237.
(49) Aoki, K.; Akimoto, K.; Tokuda, K.; Matsuda, H.; Osteryoung, J. *J. Electroanal. Chem.* **1984**, *171*, 219.
(50) Coen, S.; Cope, D. K.; Tallman, D. E. *J. Electroanal. Chem.*, in press.
(51) Winograd, N.; Blount, H. N.; Kuwana, T. *J. Phys. Chem.* **1969**, *73*, 3456.
(52) Blount, H. N.; Winograd, N.; Kuwana, T. *J. Phys. Chem.* **1970**, *74*, 3231.
(53) Rashid, A.; Kalvoda, R. *J. Electroanal. Chem.* **1970**, 28, 245.
(54) Fleischmann, M.; Lasserre, F.; Robinson, J.; Swan, D. *J. Electroanal. Chem.* **1984**, *177*, 97.
(55) Joslin, T.; Pletcher, D. *J. Electroanal. Chem.* **1974**, *49*, 171.
(56) Feldberg, S. W. *J. Electroanal. Chem.* **1981**, *127*, 1.
(57) Varco Shea, T. Ph.D. Dissertation, The University of Texas at Austin, 1987.

RECEIVED for review November 20, 1986. Accepted May 1, 1987. The support of this research by the National Science Foundation (CHE 8402135) is gratefully acknowledged.

Catalytic Oxidation of Reduced Nicotinamide Adenine Dinucleotide at Hexacyanoferrate-Modified Nickel Electrodes

Bernadette F. Y. Yon Hin and Christopher R. Lowe*

The Biotechnology Centre, University of Cambridge, Downing Street, Cambridge CB2 3EF, United Kingdom

The redox mediator hexacyanoferrate(II/III) has been electrodeposited on nickel by anodization of porous nickel electrodes in aqueous electrolytes containing hexacyanoferrate(II) ions. Cyclic voltammetry of the resultant nickel hexacyanoferrate films reveals the presence of two peaks corresponding to the hexacyanoferrate(II/III) redox couple. The redox films catalyze the oxidation of reduced nicotinamide adenine dinucleotide (NADH) with a decrease in overvoltage of ~150 mV compared to unmodified electrodes. The steady-state current response at +0.2 V vs. Ag/AgCl in 0.1 M sodium perchlorate containing 0.01 M sodium phosphate, pH 7.5, increases linearly with NADH concentration. The nickel hexacyanoferrate films are capable of reoxidizing enzymically generated NADH. In the presence of soluble or immobilized alcohol dehydrogenase, a rapid rise in current was observed after addition of ethanol, reaching steady state within 30–60 s. The hexacyanoferrate-modified nickel electrode possesses many of the features desirable for use as an amperometric sensor for oxidoreductase substrates.

Dehydrogenases constitute an important class of redox enzymes that use the cofactor β-nicotinamide adenine dinucleotide (NAD^+) and produce the reduced form NADH. Recently, much effort has been directed toward the electrochemical oxidation of NADH, in order to develop amperometric enzyme electrodes for substrates which are enzymatically coupled to NAD^+/NADH (*1*, *2*) or to regenerate electrochemically the cofactor for enzymatically coupled biotransformations (*3*, *4*). The amperometric electrodes combine the specificity and selectivity of biological molecules with the direct transduction of the rate of the reaction into a current response and represent powerful tools in the field of analysis and biotechnology.

However, direct NADH oxidation at solid electrodes takes place at considerable overpotentials, 1.1 V at carbon (*5*) and 1.3 V at platinum electrodes (*6*). Furthermore, it has been reported that the reaction involves radical intermediates which cause electrode fouling (*7*). Consequently, redox mediators have been investigated as a means of shuttling electrons between the NADH molecules and the electrode at lower overpotentials. A number of homogeneous electron-transfer mediators such as *o*- and *p*-quinones, phenazine methosulfate (PMS), (2,6-dichlorophenol)indophenol, and Meldola Blue have been used successfully to oxidize NADH (*8–13*). Subsequently, the strategy has been to design chemically modified electrodes that would provide surface-immobilized redox functionalities to catalyze efficiently the NADH oxidation (*14–19*). Such catalysis has been achieved, although the commonest problem encountered has been the poor stability

0003-2700/87/0359-2111$01.50/0